Title

Non-canonical Receptive Field Properties and Neuromodulation of Feature-Detecting Neurons in Flies

Journal

Current Biology, 30(13)

ISSN

0960-9822

Authors

Städele, Carola
Keleş, Mehmet F
Mongeau, Jean-Michel
et al.

Publication Date

2020-07-01

DOI

10.1016/j.cub.2020.04.069

Peer reviewed

HHS Public Access

Author manuscript

Curr Biol. Author manuscript; available in PMC 2021 July 06.

Published in final edited form as:

Curr Biol. 2020 July 06; 30(13): 2508–2519.e6. doi:10.1016/j.cub.2020.04.069.

Non-canonical receptive field properties and neuromodulation of feature detecting neurons in flies

Carola Städele[1,2], **Mehmet F. Keleş**[1,3], **Jean-Michel Mongeau**[1,4], **Mark A. Frye**[1,*]

[1]Department of Integrative Biology and Physiology, University of California Los Angeles, Los Angeles, CA 90095-7239, United States

[2]Present address: School of Biological Sciences, Illinois State University, Normal, IL 61790-4120, United States

[3]Present address: Department of Neurology, Johns Hopkins University, Baltimore, MD 21205, United States

[4]Present address: Department of Mechanical Engineering, Pennsylvania State University, University Park, PA 16802, United States

SUMMARY

Several fundamental aspects of motion vision circuitry are prevalent across flies and mice. Both taxa segregate ON and OFF signals. For any given spatial pattern, motion detectors in both taxa are tuned to speed, selective for one of four cardinal directions, and modulated by catecholamine neurotransmitters. These similarities represent conserved, canonical properties of the functional circuits, and computational algorithms for motion vision. Less is known about feature detectors, including how receptive field properties differ from the motion pathway, or whether they are under neuromodulatory control to impart functional plasticity for the detection of salient objects from a moving background. Here, we investigated 19 types of putative feature selective lobula columnar (LC) neurons in the optic lobe of the fruit fly *Drosophila melanogaster* to characterize divergent properties of feature selection. We identified LC12 and LC15 as feature detectors. LC15 encodes moving bars, whereas LC12 is selective for the motion of discrete objects, mostly independent of size. Neither is selective for contrast polarity, speed, or direction, highlighting key differences in the underlying algorithms for feature detection and motion vision. We show that the onset of background motion suppresses object responses by LC12 and LC15. Surprisingly, the application of octopamine, which is released during flight, reverses the suppressive influence of background motion, rendering both LCs able to track moving objects superimposed against background

AUTHOR CONTRIBUTIONS

C.S. designed experiments, collected LC imaging screen data, performed imaging and immunohistochemistry experiments, analyzed data, prepared figures, and wrote the paper; M.F.K. designed experiments, provided code and reagents, and edited the paper; J.M.M. collected LC imaging screen data; M.A.F. acquired funding, conceived the scope of work, designed experiments, provided supervision, and wrote the paper.

*Lead contact: frye@ucla.edu

DECLARATION OF INTERESTS

The authors declare no competing interests.

motion. Our results provide a comparative framework for the function and modulation of feature detectors and new insights into the underlying neuronal mechanisms involved in visual feature detection.

eTOC blurb

What are the neuronal mechanisms for extracting visual features? Städele *et al.* examine a group of 19 neuron classes of the fly brain and highlight two that detect visual features with response properties very different from those that characterize motion vision. Feature detection by these cells is under neuromodulatory influence by octopamine.

Keywords

object vision; motion vision; visual processing; octopamine; lobula columnar neurons; visual projection neurons

INTRODUCTION

The adage “A picture is worth a thousand words” highlights the economy of visual information. A commonplace visual function is the perception of the features that discriminate salient objects from a complex background scene. Salient features can include color, contrast, shape, size, orientation, texture, or relative motion. Feature-detecting visual projection neurons (VPNs) encode and convey this information between brain areas and have been identified in a variety of animals including frogs [1], feline cortex [2,3], mouse superior colliculus [4,5], zebrafish tectum [6], the optic lobe of dragonflies, blowflies, hoverflies [7–10], and fruit flies [11–14]. The seemingly ubiquitous presence of feature detecting VPNs in a wide variety of taxa emphasizes the evolutionary pressure for this form of visual processing. Yet the computational structure, connectivity, and modulation of feature detectors remain poorly understood by comparison to the heavily investigated mechanisms for motion vision [15–17]. Comparisons between the two could provide fundamental insights.

Motion vision seems to be a broadly conserved neural computation as evidenced by striking similarities between flies and mammals including parallel neuronal circuits for computing the movement of dark (OFF) edges and bright (ON) edges, and selectivity by individual cells for motion in one of four orthogonal directions [18]. Due to these similarities, great strides have been made in elucidating the circuits underlying these computations. Circuit connectivity, however, cannot fully explain motion vision, as neither the mammalian nor insect visual system is functionally ‘hard-wired’ [19,20]. The mammalian retina is richly innervated by catecholaminergic neurons releasing dopamine, epinephrine, and norepinephrine [21]. In flies, the analog of norepinephrine, octopamine, acts to increase the response gain and frequency sensitivity of motion-detecting neurons as well as every upstream input tested to date [20].

In flies, numerous putative feature detecting VPNs have been identified in the fourth optic ganglion, the lobula [12,22–25], including the lobula columnar neurons (LCs, ~20 types).

Each LC class comprises 20 to 200 columnar copies [12]. LC dendrites tile the visual field and the synaptic terminals form discrete glomerular structures where retinotopy is lost [11,12,26]. Recent studies have begun to explore the functional properties of LC neurons and their responsiveness to visual features such as looming, edge motion, and small object motion [11–13,26–30], but the functional properties of many of these LCs, their selectivity for the visual features that draw flies' attention, and whether they share conserved properties of motion vision, remains unresolved.

Here, we initiated a functional screen of 17 LC and 2 lobula plate lobula columnar (LPLC) neuron classes for physiological responses to visual stimuli that evoke robust tracking of a vertical bar [31,32], avoidance of a small object [31,33,34], and smooth fixation of a drifting wide-field panorama [35,36]. Upon identifying LC classes that responded vigorously to these stimuli, we comprehensively analyzed the receptive field properties using stimulus parameters that characterized defined circuits in the motion pathway. Finally, we test the hypothesis that octopamine modulates visual response gain, similar to the motion pathway [37–39]. We found that the receptive field properties and LC neuromodulation differ qualitatively from the canonical properties of the motion pathway.

RESULTS

We use the terms 'wide-field' or 'panoramic' to refer to visual stimuli, such as periodic gratings, that extend over the entire elevation and azimuth of our display to stimulate a large portion of the visual field. The terms 'object' and 'figure' refer to stimuli that differ from the visual background and only stimulate a small visual field. A vertical bar and a small square are objects.

Several LC types show responses to vertical bars and small objects

We screened 19 identified types of VPNs [12,23,24] for visual responses to three classes of visual stimuli we refer to as standard stimuli: a dark 8.8×8.8° small object, a dark 8.8×70° vertical bar against a uniformly lit background, and periodic wide-field grating (period 17.6°). All stimuli moved at 22°/s (grating temporal frequency 1.25Hz). These stimuli are shown to evoke robust visuomotor behaviors in walking and flying flies [31,33,34]. The screen included 17 LC neurons and 2 LPLC neurons. We exclusively used split-GAL4 driver lines because of their high specificity for the respective class of neurons. Visually evoked GCaMP6f responses from head-fixed flies were recorded using two-photon calcium imaging (Figure 1A). Stimuli were projected onto a cylindrical arrangement of light-emitting diodes, and recordings were performed in the right optic lobe (Figure 1B). We recorded population activity of a given LC type by imaging from the axon terminals forming a glomerulus in the ventrolateral protocerebrum (VLP, Figure 1C, S1B–C). Although this is a small stimulus set, we were surprised to find that only five out of the 19 screened LC types responded to the bar or small object stimuli (Figure 1D). LC15 responded mainly to the vertical bar, LC12 and LC16 responded to both the bar and the small object, and LC11 and LC26 responded only to the small object. None of the 17 LC and 2 LPLC types showed strong responses to the wide-field grating.

Qualitatively, response profiles generated with solid dark objects agreed with experiments in which we controlled for spatial luminance cues with randomly textured objects moving against a similar random background – the object disappears if it stops moving (Figure S1A). Most tested LC types showed similar responses to motion-defined objects (Figure S1A) and luminance-defined objects (Figure 1D). LC16 and LC26, however, respond only to luminance-defined objects. LC16, as well as LC4, LC6, and LPLC2, have been previously shown to be excited by a looming solid disk, or a single edge of the disk [12–14,30]. LC10a responds to 10° square objects [29], but our driver labels LC10b [12], which is not excited by small objects (Ines Ribeiro personal communication). Because LC16 or LC26 did not generalize luminance- and motion-defined objects, we did not explore these LC types further. LC12 has been explored previously, but only with bar or edge stimuli [27], not small objects. LC11 has been comprehensively described previously [11]. We therefore focused on LC12 and LC15, as well as novel results of two experiments with LC11. We have addressed the following questions: 1) What are the cellular inputs to LC12 and LC15, and what information is conveyed within the postsynaptic dendrites? 2) Which visual features of an object do LC12 and LC15 respond to, and what are the receptive field properties?

Presynaptic activity evoked by small object motion is localized to lobula layers 2/3

Identifying the presynaptic inputs is crucial to understanding the mechanism for feature detection by higher-order LC projection neurons. We devised a computational approach to screen >3500 registered Janelia GAL4 driver lines [40] for neurons that arborize within lobula layers 2 to 4, where LC12 and LC15 postsynaptic arbors are located. We focused on lines originating in the medulla or lobula plate. The screen identified 300–400 candidate input lines, and we selected roughly 50 lines to test for LC connectivity. Our screen included T2 and T3 neurons, which are shown to be highly sensitive to small objects and to innervate LC11 [41], as well as T4 and T5 motion-detecting neurons [42]. Our screen most likely did not include Tm2, Tm3, Tm4, or Tm9. To determine whether a candidate line is synaptically connected to one of the LC neurons, we tested for anterograde trans-Tango labeling [43] of LC glomeruli that can be readily identified by their shape and location in the VLP [25]. Unfortunately, none of the selected lines labeled LC12 or LC15 glomeruli (data not shown), including T2, T3, T4, and T5 neurons, which is noteworthy given the broad interest in these cells. These negative results suggest that neither LC12 nor LC15 receive direct synaptic inputs from any of the T neurons and may instead rely heavily on indirect innervation pathways. Near-future electron microscopy reconstruction results identify direct LC input partners and indirect circuits.

Our failure to identify potential input neurons motivated us to revisit the distribution of pre- and postsynaptic LC neuron arborizations across lobula layers. Prior immunohistochemical studies indicate a layer-specific neuropharmacological organization in the lobula. Lobula layers 2 and 3, for example, show enriched GABAergic signaling [44], and layers 1 and 4 seem to be enriched with cholinergic structures [45]. Confirming work by Wu and colleagues [12], co-labeling with DenMark and synaptotagmin (syt.eGFP) [46] revealed that LC12 has no presynaptic sites in the lobula (Figure 2A). Postsynaptic arbors were mainly concentrated in lobula layers 2 and 4, with sparse arbors in layer 3. Figure 2B summarizes the known arbor distribution for all LC neurons identified by our screen responsive to both

motion-defined and luminance-defined objects (LC11, LC12, LC15, Figure 1D, S1A), plus two others that respond to luminance-defined solid objects only (LC13, LC16, LC26, Figure 1D). Whereas the distribution of pre- and postsynaptic arbors for each of these LC types is complex, only LC11, LC12, and LC13, which are generally responsive to small moving objects, possess postsynaptic arbors within lobula layer 2 (Figure 2B). We thus tested the hypothesis that motion-defined small object signals are conveyed selectively to lobula layer 2. We expressed synapse-localized GCaMP6s within a pan-neuronal driver line (R57C10-GAL4) and imaged presynaptic calcium activity in the lobula evoked by our three test stimuli. We compiled maximum intensity projections within a narrow strip orthogonal to the layers of the lobula (Figure 2C). Figure 2D shows data from three out of ten flies. Subtraction of the bar response profile from the object response revealed that in each preparation the small object strongly activated layer 2 and, in many preparations, also layer 3 (Figure 2D and E, obj-bar, Figure S2). By contrast, we did not find consistent layer-specific activation by the bar. Activation by the wide-field grating was restricted mainly to layer 1 (Figure 2F), which is innervated by columnar T5 motion detectors [12]. Notably, columnar medulla T2a (misidentified in [41] as T2) innervates layers 2/3, and T3 neurons innervate layer 3 [22]. T2 and T3 are both sensitive to ON and OFF flashes, selective for small objects, and show trans-Tango labeling of LC11 [41], but not LC12 and LC15. Thus, if LC11, LC12, and LC15 pool from any common upstream pathways, they are likely complex and indirect.

LC12 and LC15 are ON-OFF object motion detectors

To better understand the visual properties of LC12 and LC15, we first tested contrast polarity preferences by using an 8.8×70° bright and dark vertical bar that moved 22°/s horizontally over the display. Previous experiments showed that LC12 and LC15 responded strongly to this bar size (Figure 1D). In both LCs, the time series of GCaMP6f responses were similar for the brightest ON, and the darkest OFF bar (Figure 3A) and peak responses were not statistically different from each other (Figure 3A’). Parameterizing the Weber contrast indicated that LC12 and LC15 are selective for high contrast, regardless of polarity (Figure 3B, B’). Neither LC12 and LC15 showed contrast polarity differences and are thus equally sensitive to bright or dark objects.

LC11 has been shown to detect only small objects when they are moving [11]. We tested if LC12 and LC15 show a similar motion selectivity by comparing GCaMP6f responses of a moving dark bar (8.8×70°, 44°/s velocity) to the appearance (OFF transient) and disappearance (ON transient) of a static flicker. The temporal frequency of the ON and OFF transients of the static flicker coincided with the edge transitions imposed by the moving bar. Our data reveals that LC12 and LC15 are both movement detectors. Both the average time course of GCaMP6f activity (Figure 3C) and the peak response amplitude (Figure 3C’) indicate that LC12 and LC15 are significantly more responsive to a moving bar than to the flicker generated by its edges.

LC12 dendrites span more columns than its receptive field whereas LC15 dendrites span fewer

The relationship between dendritic span and receptive field size could inform structure-function relationships. We, therefore, revisited LC12 and LC15 anatomy by performing multicolor stochastic labeling of single LC neurons (MCFO-1, [47]) and counted how many lobula columns are covered by the dendrites of individual cells (Figure 4A). Similar to results described by Wu and colleagues [12], we found that the dendrites of individual LC12 neurons spanned on average five columns in the anteroposterior axis (5.2±1.2 columns) and three columns in the dorsoventral axis (3.3±0.7 columns, N=9 flies, >50 cells). Considering that each column samples ~5° of the visual field, the LC12 dendritic span corresponds to ~26×16°. By contrast, individual LC15 dendrites spanned on average five columns in the anteroposterior axis (5.3±0.6 columns) and five columns in the dorsoventral axis (5.1±0.9 columns, N=11 flies, >50 cells), corresponding to ~26×25°,.

We next sought to characterize the receptive field (RF) size of individual LC12 and LC15 neurons. We measured single-cell responses of individual LC neurons within the LC cluster by recording calcium responses of individual neurites in the lobula (Figure 4B) in response to a 2.2° dark bar displaced in 13° increments in each cardinal direction (see Star Methods). In short, the 105×66° arena test area was binned into eight azimuthal and five elevation sampling bins (Figure 4C). For all tested LC12 neurons, the RF of individual neurites was very small, on the order of a single 13° sampling bin (Figure 4C). By contrast, the RF of individual LC15 neurites comprised at least three bins in the vertical and horizontal direction (Figure 4D). To determine the average RF size across animals, we spatially normalized to the bin that showed the strongest calcium responses (bin 0 = RF center) and plotted the surrounding responses relative to bin 0 (Figure 4C', D'). LC15 neurites with their RF occluded by the display boundary were excluded from the analysis. RF sizes for both LC types were consistent within and across animals. On average, LC12 receptive field was 13° or smaller (Fig 4'), whereas LC15 receptive field was ~40° in the horizontal and vertical direction (Figure 4D'). RF centers for both LCs were distributed across the visual field (Fig 4C", D").

The difference in RF size between LC12 and LC15 could explain why there are about 200 copies of LC12 neurons to sample the full visual field, by comparison to about 70 copies of LC15 neurons. When comparing the RF sizes with the dendritic span, we found that individual LC12 dendrites span about twice as many columns in the anteroposterior axis as the receptive field (26×16° dendritic span versus 13×13° RF), suggesting that dendrites of individual LC12 neurons are overlapping by about 50% and might thereby receive spatial inhibition. We found the opposite for LC15 in which individual LC15 dendrites cover only 60% of the RF (26×25° dendritic span versus 40×40° RF).

LC12 is a speed-insensitive horizontal motion detector, while LC15 is a speed-insensitive omni-directional motion detector

Motion detectors show strong preferences for stimulus direction [3,42,48]. We tested whether LC12 or LC15 show directional selectivity. From the data collected during the RF scan, we extracted the maximum GCaMP6f responses of individual neurites to the

movement of a 2.2° wide dark bar in each of the four cardinal directions (22°/s velocity). We found that LC12 responded equally to motion in either direction along the horizontal axis (Figure 5A, top) but was almost insensitive to motion in the vertical axis. The RF size and dendritic span of individual LC12 neurons might explain this finding. Both are small in the vertical dimension. It seems plausible that there is little vertical dendritic overlap between adjacent LC12 neurons, which would explain why individual LC12 neurons are only responsive to a small spot (13°) along this dimension. By contrast, LC15 appeared to be omnidirectional and showed the same response amplitude to motion in all four directions (Figure 5A, bottom).

The velocity of behaviorally relevant signals is an essential parameter for behavioral control. An object that approaches quickly elicits an escape response while a slow approaching object might be ignored. We tested speed dependence in LC12 and LC15 by using an 8.8×70° dark bar moving horizontally from front to back with velocities ranging from 22 to 132°/s. Average peak calcium responses in both LC12 and LC15 were not statistically different across this speed range (Figure 5B), which contrasts with LC11 that shows a monotonic increase in response amplitude, peaking at 220°/s [41]. The flat velocity profile could reflect neuronal saturation driven by high contrast stimuli. We noted, however, that although peak amplitude was insensitive to speed, GCaMP6f response duration was correspondingly larger for slow motion and shorter for fast motion (Figure 5C). Slower stimuli are displayed over a longer time than faster stimuli.

LCs show complex combinations of spatial inhibition and spatial saturation

Most of the visual stimuli used to this point comprised 8.8° wide vertical bars or small objects. We next tested for object size tuning of both LCs. We recorded population activity from the presynaptic glomerulus in response to objects of varying height and width. For LC12, GCaMP6f response amplitude increased with object height and saturated for bars 35° or taller (Figure 6A, top). By contrast, LC15 responses increased monotonically with object height and did not reach a plateau (Figure 6A, bottom). Thus, neither LC12 nor LC15 appeared to be size tuned in the vertical dimension, suggesting that there is no surround inhibition impinging upon the RF. The decreased response latency of LC15 with bar height could reflect the spatial organization of the receptive fields being pooled in the glomerulus, or instead, be due to taller objects moving further into an asymmetric receptive field. Our data reject the latter conclusion because the receptive fields are relatively symmetrical (Figure 4D, D”) and do not become asymmetrical in the peripheral areas of the lobula. Since both LCs showed strong responses to bars, we used this stimulus to test for width preference. Systematically varying bar width revealed some peculiar differences between the two LCs. Peak amplitude responses by LC12 were rather flat for increasing bar width, but the duration of the response increased (Figure 6B, top). By contrast, LC15 showed classical size tuning in the horizontal dimension, with peak amplitude responses for the smallest bars and decreasing to less than half maximum for bars 18° or wider (Figure 6B, bottom).

The systematic increase in the temporal duration and dual peaks in GGaMP6f responses to wide bars (Figure 6B) motivated us to examine whether signaling in the terminal glomerulus reflected two discrete ‘waves’ of activity within the dendrites corresponding to the leading

and trailing edges of a wide bar. We recorded from single dendritic neurites in the lobula to bars of two different widths (4.4° and 70°). For both LCs, the narrow bar generated a single GCaMP6f peak, whereas the wider bar generated discrete full-amplitude responses to both the leading and trailing edges (Figure 6C, C'). Equivalent response amplitude to the OFF and ON edges of the dark bar support the lack of selectivity for contrast polarity in these LCs (Figure 3B, B'). The narrow bar elicited half-maximum response duration on average 0.7±0.2s longer for LC12 (7 flies, 20 dendrites) and 0.6±0.1 s longer for LC15 (7 flies, 19 dendrites) than the response to the leading edge of the wide bar. This suggests that both LCs responded to the leading and trailing edges of the 4.4° narrow bar, but the GCaMP6f decay kinetics effectively fused these dynamics. In summary, we have found that both LC12 and LC15 show no clear height tuning but that LC15 showed the strongest responses to bars narrower than 8.8°. Table S1 summarizes all visual response properties of LC12 and LC15.

Octopaminergic neuromodulation enables object detection against background motion

A potent property of some feature detectors is their ability to distinguish object motion against the background optic flow generated when the observer is moving [5,9,49,50]. For LC11, however, the onset of background motion suppresses small object responses [41], implying that this cell class is only effective for object motion detection when the animal is stationary. We tested whether similar response suppression by background motion occurs in LC12 and LC15 by presenting an 8.8×70° dark bar moving at 44°/s over a low contrast background grating. In both LC12 and LC15, bar responses were rapidly and significantly suppressed by concomitant background grating motion (Figure 7A, A').

Recent studies have shown that the baseline membrane potential and visually evoked responses of visual neurons can be influenced by the animal's locomotor state [39,51]. On flight initiation, the nervous system of *Drosophila* is flushed with the biogenic amine octopamine, which increases the response gain of motion-sensitive neurons in the medulla and lobula plate [20]. To test the hypothesis that octopamine modulates the function of LC12 and LC15, we bath-applied the octopamine agonist chlordimeform [52] (CDM, 100 μM) and repeated the previous experiment. CDM application did not significantly alter either LC12 or LC15 responses to a dark bar presented over a low contrast stationary grating (Figure 7B, bar only). To our surprise, however, CDM application reversed the suppression of bar responses by superimposed background grating motion. In CDM, LC12 mean response amplitude was restored to that evoked by bar motion alone (Figure 7B, bar+bkg). Bar responses by LC15 were only partially restored but were significantly larger in CDM than in the saline control (Figure 7B'). We found qualitatively similar results for experiments in which wide-field motion was initiated midway through a bar response, or for experiments in which we varied the direction of bar and background motion (Figure S3). To test whether the influence of CDM is widespread among feature detecting LCs, we repeated the experiment with LC11 using an 8.8° dark square object moving at 44°/s over a background grating. CDM application had no significant influence on object motion responses with a stationary grating, nor did CDM alter the fully suppressive effect of wide-field grating motion on LC11 small-object responses (Figure 7C, C').

DISCUSSION

In addition to their selectivity for sophisticated features of moving stimuli such as small objects or bars, lobula columnar projection neurons show RF properties and aminergic neuromodulation that differ markedly from motion vision circuits, adding a layer of complexity to visual processes that may be broadly shared across taxa.

Object detecting LCs are broadly indifferent to object contrast polarity, movement direction and velocity

In flies, as in mammals, photoreceptor signals are multiplexed into two parallel half-wave rectified contrast polarity channels for ON and OFF edges [53–55]. These pathways culminate with columnar motion detectors selective for moving ON edges (T4) and OFF edges (T5) [56]. Neither of the LCs tested here showed contrast polarity selectivity (Figure 3A, B). Interestingly, the medulla columnar neurons T2a and T3 project to lobula layer 2/3 and innervate the small-object selective motion detector LC11. LC12 and LC15 are similarly agnostic for contrast polarity as LC11 [11], acting instead as full-wave rectifiers of luminance changes [41]. A proposed elementary feature detector rectifies inputs for the temporal correlation of ON and OFF sequences at a single point in space [57,58]. A visual computation dependent upon a single spatial input would be directionally non-selective by definition. By contrast to individual columnar T4 and T5 motion detectors that are selective for one of four orthogonal directions of motion [56], columnar LC12 and LC15 neurons show no directional selectivity (Figure 5A), similar to LC11 [11]. The peculiar structure of axial directional tuning in LC12 might indicate strong orientation selectivity, which enhances directional selectivity in T4/T5 [59]. However, GCaMP6f responses by LC12 to a static bar oriented orthogonal to its preferred motion axis (Figure 3C, C’) are weak by comparison to T4/T5.

For a fixed spatial pattern, motion detectors are speed tuned. When presented with a single-pixel bar on a similar LED display over a similar speed range as used here, T4 motion detectors show clear response tuning to the velocity of a periodic grating with peak responses at ~28°/s [60]. By contrast, LC12 and LC15 show an even distribution of max ‘F/F responses between 22–132°/s (Figure 5B). Likewise, small target motion detectors (STMDs) of the hoverfly lobula show broad velocity tuning, with spiking frequency constant between 20–120°/s [9]. Nevertheless, STMD neurons can provide unambiguous information about object velocity. The number of spikes scales linearly with object speed in STMDs [61]. Similarly, the duration of GCaMP6f responses by LC12 and LC15 diminish with increasing speed (Figure 5C), indicating that total calcium accumulation and, therefore presynaptic release may scale with speed.

LC12 and LC15 show complex relationships between spatial dendritic span and receptive field size

To understand the lateral spread of visual signals, a comparison of the RF and dendritic spread of a neuron is useful. The input dendrites of T4 and T5 neurons span at least seven columns in a hexagonal array, equivalent to 15° of visual space [62], corresponding well with the 20° functional RF [63]. By contrast, LC11 has a much larger dendritic span than RF

[11]. LC12 dendrites sample roughly twice as many columns as the RF would predict, while LC15 dendrites span only 60% (Figure 4C', D'). It would be tempting to speculate that size tuning by inhibition requires columnar inputs surrounding the classical RF, which would be supported by the exquisite size tuning in LC11 (strong surround inhibition). However, LC12 responses saturate once the RF is filled (no surround inhibition), and LC15 shows horizontal size tuning (Figure 6B), but its dendritic span undersamples the RF (Figure 4D'). Future work on subcellular synaptic connectivity and transmitter identity will resolve these complexities.

LCs show qualitative functional shifts by neuromodulation

Visual processing in insects is remarkably plastic and can be regulated by chemical neuromodulators, cross-modal sensory inputs, and internal states [20]. Octopamine has long been associated with homeostatic responses to the amplified metabolic and cell-energetic demands of insect flight [64]. In the motion vision pathway, bath applied octopamine (or its agonist chlordimeform [52]) increases the amplitude of visually evoked responses by medulla interneurons, slightly shifts the frequency sensitivity of postsynaptic small-field T4/T5 motion detectors, and increases the amplitude and shifts frequency sensitivity in wide-field motion detectors of the lobula plate [38,39,65,66].

Octopamine seems to modulate neurons of the motion pathway quantitatively by increasing visual response gain, but without changing RF size or other qualitative characteristics [65]. By contrast, octopamine changes the qualitative structure of LC12 and LC15 responses by enhancing object detection against a moving panorama (Figure 7). Recent work has revealed striking effects of octopaminergic neuromodulation on behaviors driven by visual features. *Drosophila melanogaster* instinctively avoid small moving objects in flight [33]. Yet, optogenetic stimulation of octopaminergic neurons reverses object aversion to approach [34]. Signals from looming detectors LC4 and LPLC2 are only transmitted to a pair of descending neurons (DNp07, DNp10) when the animal is flying, or octopamine is bath applied [51]. How LC12 and LC15 participate in object behaviors in Drosophila is unknown, yet octopamine mediated object detection is reminiscent of the dragonfly lobula STMD neuron CSTMD1 [57,67], which responds to a small contrasting target even it is presented against a moving panoramic background [68]. Future work can uncover the presynaptic inputs, visual processing algorithms, and integration sites with the motion vision pathway to illuminate the mechanisms underlying the rich repertoire of visual behaviors that flies possess.

STAR METHODS

RESOURCES AVAILABILITY

Lead contact—Further information and requests for resources and reagents should be directed to and will be fulfilled by the Lead Contact, Mark Frye (frye@ucla.edu).

Materials availability—This study did not generate new unique reagents.

Data and Code Availability—The datasets and MATLAB analysis code used for this study are available at Mendeley Data (doi: 10.17632/ssgpb4wmh9.1).

EXPERIMENTAL MODEL AND SUBJECT DETAILS

Fly stocks and handling—Calcium imaging and anatomy experiments were performed with female *D. melanogaster* flies 3–5 days after eclosion, maintained under standard conditions (25°C, 30–50% humidity, 12h light/dark cycle, standard cornmeal food). To genetically target LC neurons we exclusively used split-GAL4 [69,70] driver lines because of their high specificity for the respective class of neurons. Fly driver lines were crossed with fly effector lines (Key Resources Table, and Table S1), and the progeny was used for experiments.

LC12 and LC15 driver lines—OL0042B [12] was used as a driver line to genetically target LC15. Two different driver lines were used to genetically target LC12: OL0007B and OL0008B [12]. Both LC12 driver lines are highly specific and show no off-target labeling in 3–5 days old flies in the lobula or the ventrolateral protocerebrum (VLP) where LC12 axons terminate in an optic glomerulus. We compared calcium responses of OL0007B and OL0008B and found no statistically significant difference in response amplitude or dynamics. For experiments where LC12 responses are recorded but not manipulated (as in our study) both lines can be used interchangeably. We found for flies that are older than ~14 days, the OL0007B driver showed weak labeling in LC10 as well. Calcium imaging experiments were performed using either OL0007B or OL0008B but all anatomical data were collected using only OL0008B.

METHOD DETAILS

Solutions—*D. melanogaster* saline was composed of (in mM): 103 NaCl, 3 KCl, 1.5 $CaCl_2$, 4 $MgCl_2$, 26 $NaHCO_3$, 1 NaH_2PO_4, 10 trehalose, 10 glucose, 5 TES, 2 sucrose, adjusted to 273–275 mOsm, pH 7.3. For pharmacological experiments, agonists were prepared from concentrated stock solutions immediately before the experiment. Stock solutions were stored at −20°C in small quantities and diluted in *D. melanogaster* saline to the final concentration. Chlordimeform (Sigma-Aldrich, 31099) was prepared as a 1mM stock solution in ultrapure water (18.3 MΩ, Millipore) and used at a final concentration of 100μM. Measurements were taken after 15min wash in.

Fly preparation for optical imaging—Female flies were anesthetized at 4°C on a cold plate and mounted to a 3D printed fly holder (modified from [71]) using ultraviolet glue (Dreve Fotoplast gel, Audiology Supplies, 44811). The fly's legs were immobilized with low melting point beeswax to eliminate interference with recordings and visual stimulation. Fine forceps (Dumont, #5SF, Fine Science Tools) were used to remove the cuticle on the posterior surface of the fly's head to expose the right optic lobe in the region of the lobula and VLP (Fig 1B, 1C).

Two-photon optical imaging—During two-photon imaging the brain was continuously perfused with fly extracellular saline at 1.5 ml/min via a computer-controlled system (VC-6, Warner Instruments). Bath temperature was kept at 20°C with an inline-solution heater

(SC-20, Warner Instruments) and a temperature controller (TC-324, Warner Instruments). LC neurons were imaged at 920nm using a Ti:Sapphire pulse laser (Coherent, Santa Clara, CA) controlled by SlideBook (Version 6, 3i, Boulder, CO). We imaged with a 20x water-immersion objective (W Plan Apochromat, 1.0 DIC, Zeiss) with three layers of blue filter (Indigo, Rosco, No. 59) to reduce bleed-through from the LED arena to the photomultipliers. Single plane images were taken at 10 frames/s with each frame at a x-y pixel resolution ranging from 150×256 to 168×212 and 0.2 to 0.3 μm pixel spacing. To record population responses of a given LC type, GCaMP6f responses were recorded in the LC output glomeruli where all terminals merge together. To record activity of single LC neurons, GCaMP6f responses were measured from individual dendritic neurites in the lobula.

Visual Stimulation—Visual stimuli during two-photon imaging were presented on a cylindrical LED arena [72]. The arena was composed of 4 rows and 12 columns of 8×8 LED dot matrix panels (470nm, Dongguan Houke Electronic Co., 12088-AB). The LED display covered +/−108° of the visual field in the horizontal, and +/−35° in the vertical dimension. Each pixel subtended 2.2° on the fly's retina at the visual equator. Stimuli were generated and controlled using custom MATLAB scripts. The two dorsoventral corners of the LED arena were occluded from the fly's field of view by the tethering stage [73]. Thus, a bar moving back to front on the display ipsilateral to the recording site does not reach its full height for the first ~10° excursion. Schematic representations of the visual stimuli in the figures are therefore depicted as trapezoids.

Visual stimuli were grouped into sets such that each set encompassed a single block of trials, presented in random block design. To reduce onset artifacts, all motion stimuli included a 4 second pre- and post-stimulus epoch where the background illumination was set to 50% of the maximum LED intensity. We waited at least 8 seconds between stimuli to allow cellular activity to return to baseline. The arena was off throughout these inter-stimulus intervals. Visual stimulus onset times were aligned to specific imaging frames by using voltage signals that encoded pattern movement, position, and frame capture times (BNC-2090, National Instruments, 10kHz sampling rate).

Visual stimulus parameters are listed below for each figure. In most experiments we used three different types of stimuli that we refer to as standard stimuli: an 8.8°×8.8° dark object, an 8.8°×70° dark vertically elongated bar, and a grating projected across the entire display ('wide-field') with a period of 17.6°. For these stimuli, the intensity of the background was always set to 50% of the maximum LED intensity, whereas the foreground figure (small object or bar) was dark (0% intensity). For population imaging from axon terminals, each fly was presented with three repetitions of each block, trials were averaged for analysis. For dendritic and single neurite recordings, measurements were performed at different z-planes and each fly was presented with a single stimulus block at each z-plane.

In most experiments, visual stimuli were presented in multiple directions. Back to front (ipsi- to contralateral) and front to back (contra- to ipsilateral) responses were not statistically different from each other. Therefore, unless otherwise noted, we presented front to back responses (contra- to ipsilateral).

Weber Contrast (Figure 3B, B') was calculated using the following equation:

$$Weber\ contrast = \frac{I_{fg} - I_{bg}}{I_{bg}}$$

where I_{fg} is the light intensity of the foreground figure and I_{bg} the intensity of the background. In our experiments the background intensity was always set to 50%, and a Weber contrast of −1 thus corresponds to 0% LED intensity (LEDs off) of the stimulus, whereas a Weber contrast of +1 corresponds to 100% intensity.

Stimulus parameters: Figure 1D: three types of contrast defined visual stimuli, 1. dark small object, 8.8×8.8° (width × height), moving in the vertical center (equator) of the arena; 2. dark bar, 8.8×70°; 3. wide-field grating, period: 17.6°. All patterns with I_{fg}= 0%, I_{bg} = 50%, movement direction: contra- to ipsilateral, velocity: 22°/s.

Figure 2D, 2E, 2F: dark small object, 8.8×8.8°; dark bar, 8.8×70°; wide-field grating, period: 17.6°. I_{fg}=0%, I_{bg}= 50%, movement direction: contra- to ipsilateral, velocity: 22°/s.

Figure 3A: ON and OFF bar, 8.8×70°, Luminance: OFF bar, I_{fg}= 0%, I_{bg} = 50%; ON bar, I_{fg}= 100%, I_{bg} = 50%, movement direction: contra- to ipsilateral, velocity: 22°/s.

Figure 3B: bar, 8.8×70°, I_{fg} = 0–100% in 12.5% intervals, I_{bg} = 50%, movement direction: contra- to ipsilateral, velocity: 44°/s.

Figure 3C: dark bar, 8.8×70°, I_{fg}= 0%, I_{bg} = 50%, stimulus was either presented as a static flicker (bar appearing and disappearing at +26° position on the display) or moving with a constant velocity of 44°/s from the contralateral to ipsilateral arena side.

Figure 4C, 4D, 5A: dark bar, two types: 2.2×66° for horizontal movements, 105×2.2° for vertical movements, I_{fg}= 0%, I_{bg} = 50%, velocity: 22°/s, movement direction: up, down, left, right.

Figure 5B, 5C: dark bar, 8.8×70°, I_{fg}= 0%, I_{bg} = 50%, movement direction: contra- to ipsilateral, stimulus velocity: 22, 44, 66, 88, 110, 132°/s.

Figure 6A: figure height varied and was 2.2, 4.4, 8.8, 17.6, 35, 52, or 70°. Figure width was 4.4° in all conditions. I_{fg}= 0%, I_{bg} = 50%, movement direction: contra- to ipsilateral, velocity: 22°/s.

Figure 6B: figure width varied and was 2.2, 4.4, 8.8, 17.6, 35, or 70°. Figure height was 4.4° in all conditions. I_{fg}= 0%, I_{bg}= 50%, movement direction: contra- to ipsilateral, velocity: 22°/s.

Figure 6C: two types of dark bars, 4.4×70° and 70×70°, I_{fg}= 0%, I_{bg} = 50%, movement direction: contra- to ipsilateral, stimulus velocity: 22°/s.

Figure 7A, 7B: two types of stimuli, 1. dark bar, 8.8×70° moving across a stationary wide-field grating, period 17.6°; 2. dark bar, 8.8×70° moving across a wide-field grating, period

17.6°. Both stimuli with I_{fg}= 0%, I_{bg} = 25% for OFF grating and 50% for ON grating, movement direction: contra- to ipsilateral, velocity: 44°/s.

Figure 7C: two types of stimuli, 1. dark small object, 8.8×8.8° moving across a stationary wide-field grating, period 17.6°; 2. dark small object, 8.8×8.8° moving across a wide-field grating, period 17.6°. Both stimuli with I_{fg}= 0%, I_{bg} = 25% for OFF grating and 50% for ON grating, movement direction: contra- to ipsilateral, velocity: 44°/s.

Figure S1A: three types of motion defined visual stimuli, 1. randomly textured small object, 8.8×8.8°; 2. randomly textured bar, 8.8×70°; 3. randomly textured wide-field panorama. All patterns with I_{fg}= 0%, I_{bg} = 50%, movement direction: contra- to ipsilateral, velocity: 22°/s.

Figure S2: Same as Fig 2D.

Figure S3A: dark bar, 8.8×70° moving across a wide-field grating, period 17.6°. I_{fg}= 0%, I_{bg} = 25% for OFF grating and 50% for ON grating, velocity: 0 or 44°/s for bar and background. Conditions: 1. bar moving on stationary background, 2. bar and background moving from contra- to ipsilateral, 3. bar and background moving from contra- to ipsilateral but background starts to move with 3.36 s delay, 4. background only from contra- to ipsilateral, 5. bar moving from contra- to ipsilateral and background moving from ipsi- to contralateral, 6. bar moving from contra- to ipsilateral and background moving from ipsi- to contralateral but with 1.46 s delay, 7. background only from ipsi- to contralateral.

Figure S3B: same as S3A but with a dark small object, 8.8×8.8°.

Two-photon image analysis—Calcium imaging data was analyzed offline using custom written MATLAB scripts. Images were corrected for motion artifacts using a previously described algorithm [74]. Images that could not be aligned or that contained persistent motion artifacts generated by the wriggling fly were discarded. Aligned images were exported to MATLAB and ROI selection was in accord with the anatomical region that was recorded. For every pixel in this ROI mask, mean and standard deviation were calculated for the full time series. A test value for each pixel was calculated by the product of mean and standard deviation of each pixel. Pixels with test values greater than or equal to twice the mean value of all test values in the ROI mask were used for analysis. For each stimulus condition, three trials were averaged, and ΔF/F was calculated by dividing the signal by the mean intensity of the first 20 frames (2 s) preceding the stimulus motion onset.

Receptive field size and directional selectivity—To determine the functional RF size of LC12 and LC15 we measured integrated responses to a 2.2×66° wide dark bar (for left/right sweeps) and a 105×2.2° wide dark bar (for up/down sweeps) moving within 13.2° spaced bins (Fig 4B’). The bar stimulus was moved in all four cardinal directions (up, down, left, right) and the stimulus was presented only in the visible regions of the display (−26.4° to +79.2° azimuth, −35° to +35° elevation). This area was divided into eight horizontal bins (each 13.2° wide and 66° high) and five vertical bins (13.2° high, 105° wide). Stimuli were moved within the boundaries of each bin in all four cardinal directions (left and right in the horizontal bins, up and down in the vertical bins). During a sweep the bar appeared at the start of the bin, was held stationary for 1 s before moving at 22°/s to the bin end and

disappeared. Calcium responses from individual LC12 and LC15 neurons were extracted from single arbors in the lobula that showed no anatomical overlap to neighboring arbors. Only flies where the anteroposterior plane did not change during all 26 experimental conditions were included in the analysis. Neither LC12 nor LC15 showed directional selectivity in the horizontal or vertical axis and response amplitudes to left and right bar movement and up and down bar movement were almost identical. To assess the RF size, we averaged the left and right movement responses of each bin, as well as up and down responses. The averaged time series of each horizontal bin of individual neurites were multiplied with the averaged time series of each vertical bin to derive the activity matrices in Figures 4C and 4D. RF sizes across neurites showed little variation for both LC15 (~3×3 bins) and LC12 (1 bin). Maximum GCaMP6f responses always occurred in the most centered bin, thus defined as the RF center (Fig 4C", 4D"). To determine the average RF size across animals, we spatially normalized to the bin that showed the strongest calcium responses (bin 0 = RF center) and plotted the surrounding responses relative to bin 0 (Figure 4C', D'). LC15 neurites with their RF occluded by the display boundary were excluded from the analysis. Maximum GCaMP6f responses of all recorded neurites were averaged for each normalized bin separately and plotted as a heat map (Fig 4C', 4D').

Anatomy and Immunohistochemistry

Dissection: We followed standard *D. melanogaster* immunohistochemistry protocols [75]. In brief, flies were dissected in PBS and dissection time never exceeded 10 minutes. Dissected brains were placed in 4% paraformaldehyde diluted in PBS and fixed for 25 minutes at room temperature, followed by washing with PBST (0.3% v/v Triton-X100) three times for 15 minutes each. Brains were then incubated in PBST+5% normal goat serum (PBST-NGT) for 60 minutes at room temperature and incubated in primary antibodies for 2 days at 4°C diluted in PBST-NGT. Brains were then washed three times (PBST, 15 min each) and incubated with secondary antibodies diluted in PBST-NGT for 2 days at 4°C. After three more washes (PBST, 15 min each) brains were mounted on a microscope slide in Vectashield (Vector Labs, H-1000).

LC anatomy labeling: We used 3–5 days old female flies to visualize LC anatomy (Fig S1B) and the distribution of presynaptic and postsynaptic sites in the lobula (Fig 2A). Primary antibodies were anti-Bruchpilot (mouse monoclonal antibody Nc82, supernatant, Developmental Studies Hybridoma Bank, 1:10 dilution), anti-DsRed rabbit polyclonal antibody (Takara, 632496, 1:200 dilution), and anti-GFP chicken polyclonal antibody (abcam, 13970, 1:1000 dilution). Secondary antibodies used were Alexa Fluor 488 goat anti-chicken (abcam, ab150169, 1:1000 dilution), Alexa Fluor 568 goat anti-rabbit (ThermoFisher Scientific, A-11036, 1:200 dilution), and Alexa Fluor 647 goat anti-mouse (ThermoFisher Scientific, A-21236, 1:200 dilution).

Multicolor stochastic labeling of individual neurons: MCFO-1 was used (Figure 4A) and expression patterns for GAL4 lines and/or presynaptic marker distribution were performed as previously described using *pJFRC51-3xUAS-IVS-syt::smHA(attp1) and pJFRC225–5xUAS-IVS-myc::smFP-FLAG (VK00005)* as reporters. Flies were raised at 25°C and heat-shocked at 37°C for 10 min at mid-pupal stage. Eclosed flies were dissected within three

days and brains were stained following MCFO immunohistochemistry protocol as described by Nern and colleagues [47]. Primary antibodies were anti-Bruchpilot (mouse monoclonal antibody Nc82, supernatant, Developmental Studies Hybridoma Bank, 1:10 dilution) as a neuropil marker, rabbit anti-HA (Cell Signaling Technologies, 3724S, 1:300 dilution) and rat anti-FLAG (Novus Biologicals, NBP1–06712, 1:300 dilution). Secondary antibodies used were Alexa Fluor 488 goat anti-rabbit (ThermoFisher Scientific, A-11008, 1:200 dilution), Alexa Fluor 594 goat anti-rat (Jackson ImmunoResearch Lab 112-585-167, 1:200 dilution), and Alexa Fluor 647 goat anti-mouse (ThermoFisher Scientific, A-21236, 1:200 dilution).

Image acquisition: Images were acquired with an LSM700 confocal microscope using a 40x oil immersion lens (NA1.3, Zeiss). Z-stacks were acquired with a step size of 0.4–0.7 μm between optical sections. Acquired images were visualized and processed offline using Fiji.

QUANTIFICATION AND STATISTICAL ANALYSIS

We used standard statistical tests to evaluate our data, and the results are reported at the relevant locations in the figure captions. Statistics were computed in MATLAB with the Statistics toolbox. Normal distribution of data sets was tested using the Kolmogorov-Smirnov (Lillifors) test with a significance level of $p<0.01$. All presented data were normally distributed and significant differences were calculated using the paired-sample t-test or one-way ANOVA. Statistical test results are reported in APA style (t-test: *t(degrees of freedom) = t value, p = p value;* one way ANOVA: *F(degrees of freedom, residual)= F value, p = p value)*. Significant differences are stated as $*p<0.05$, $**p<0.01$, $***p<0.001$. Data collection and analysis were not conducted blind to the conditions of the experiments. N denotes the number of flies, while n refers to the number recorded of neurites or individual cells. Final figures were prepared in Adobe Illustrator CS6.

Supplementary Material

Refer to Web version on PubMed Central for supplementary material.

ACKNOWLEDGEMENTS

This work was supported by the National Institutes of Health grant R01-EY026031 to M.A.F. We thank Volker Hartenstein for use of his laboratory microscopy resources, and Ben Hardcastle for technical assistance and Fernando Vonhoff for helpful discussion.

REFERENCES

1. Lettvin J, Maturana H, McCulloch W, and Pitts W (1959). What the Frog's Eye Tells the Frog's Brain. Proc. IRE 47, 1940–1951.
2. Hubel DH, and Wiesel TN (1965). Receptive fields and functional architecture in two nonstriate visual areas (18 and 19) of the cat. J. Neurophysiol 28, 229–89. [PubMed: 14283058]
3. Hubel DH, and Wiesel TN (1962). Receptive fields, binocular interaction and functional architecture in the cat's visual cortex. J. Physiol 160, 106–54. [PubMed: 14449617]
4. Gale SD, and Murphy GJ (2014). Distinct Representation and Distribution of Visual Information by Specific Cell Types in Mouse Superficial Superior Colliculus. J. Neurosci 34, 13458–13471. [PubMed: 25274823]

5. Gale SD, and Murphy GJ (2016). Active Dendritic Properties and Local Inhibitory Input Enable Selectivity for Object Motion in Mouse Superior Colliculus Neurons. J. Neurosci 36, 9111–23. [PubMed: 27581453]
6. Preuss SJ, Trivedi CA, vom Berg-Maurer CM, Ryu S, and Bollmann JH (2014). Classification of Object Size in Retinotectal Microcircuits. Curr. Biol 24, 2376–2385. [PubMed: 25242030]
7. Egelhaaf M (1985). On the neuronal basis of figure-ground discrimination by relative motion in the visual system of the fly. II. Figure-detection cells, a new class of visual interneurones. Biol. Cybern 52, 195–209.
8. O'Carroll DC (1993). Feature-detecting neurons in dragonflies. Nature 362, 541–543.
9. Nordström K, and O'Carroll DC (2006). Small object detection neurons in female hoverflies. Proceedings. Biol. Sci 273, 1211–6.
10. Barnett PD, Nordström K, and O'Carroll DC (2007). Retinotopic Organization of Small-Field-Target-Detecting Neurons in the Insect Visual System. Curr. Biol 17, 569–578. [PubMed: 17363248]
11. Keleş MF, and Frye MA (2017). Object-Detecting Neurons in Drosophila. Curr. Biol 27, 680–687. [PubMed: 28190726]
12. Wu M, Nern A, Williamson WR, Morimoto MM, Reiser MB, Card GM, and Rubin GM (2016). Visual projection neurons in the Drosophila lobula link feature detection to distinct behavioral programs. Elife 5, e21022. [PubMed: 28029094]
13. Klapoetke NC, Nern A, Peek MY, Rogers EM, Breads P, Rubin GM, Reiser MB, and Card GM (2017). Ultra-selective looming detection from radial motion opponency. Nature 551, 237–241. [PubMed: 29120418]
14. von Reyn CR, Nern A, Williamson WR, Breads P, Wu M, Namiki S, and Card GM (2017). Feature Integration Drives Probabilistic Behavior in the Drosophila Escape Response. Neuron 94, 1190–1204.e6. [PubMed: 28641115]
15. Silies M, Gohl DM, and Clandinin TR (2014). Motion-Detecting Circuits in Flies: Coming into View. Annu. Rev. Neurosci 37, 307–327. [PubMed: 25032498]
16. Behnia R, and Desplan C (2015). Visual circuits in flies: Beginning to see the whole picture. Curr. Opin. Neurobiol 34, 125–132. [PubMed: 25881091]
17. Borst A, Haag J, and Reiff DF (2010). Fly Motion Vision. Annu. Rev. Neurosci 33, 49–70. [PubMed: 20225934]
18. Borst A, and Helmstaedter M (2015). Common circuit design in fly and mammalian motion vision. Nat. Neurosci 18, 1067–1076. [PubMed: 26120965]
19. Jacob SN, and Nienborg H (2018). Monoaminergic Neuromodulation of Sensory Processing. Front. Neural Circuits 12, 51. [PubMed: 30042662]
20. Cheng KY, and Frye MA (2019). Neuromodulation of insect motion vision. J. Comp. Physiol. A
21. Hadjiconstantinou M, and Neff NH (1984). Catecholamine systems of retina: A model for studying synaptic mechanisms. Life Sci 35, 1135–1147. [PubMed: 6147740]
22. Fischbach KF, and Dittrich APM (1989). The optic lobe of Drosophila melanogaster. I. A Golgi analysis of wild-type structure. Cell Tissue Res 258, 441–475.
23. Otsuna H, and Ito K (2006). Systematic analysis of the visual projection neurons of Drosophila melanogaster. I. Lobula-specific pathways. J. Comp. Neurol 497, 928–958. [PubMed: 16802334]
24. Strausfeld NJ, and Okamura J-Y (2007). Visual system of calliphorid flies: Organization of optic glomeruli and their lobula complex efferents. J. Comp. Neurol 500, 166–188. [PubMed: 17099891]
25. Panser K, Tirian L, Schulze F, Villalba S, Jefferis GSXE, Bühler K, and Straw AD (2016). Automatic Segmentation of Drosophila Neural Compartments Using GAL4 Expression Data Reveals Novel Visual Pathways. Curr. Biol 26, 1943–1954. [PubMed: 27426516]
26. Mu L, Ito K, Bacon JP, and Strausfeld NJ (2012). Optic glomeruli and their inputs in Drosophila share an organizational ground pattern with the antennal lobes 32, 6061–71.
27. Aptekar JW, Keleş MF, Lu PM, Zolotova NM, and Frye MA (2015). Neurons Forming Optic Glomeruli Compute Figure-Ground Discriminations in Drosophila. J. Neurosci 35, 7587–99. [PubMed: 25972183]

28. von Reyn CR, Breads P, Peek MY, Zheng GZ, Williamson WR, Yee AL, Leonardo A, and Card GM (2014). A spike-timing mechanism for action selection. Nat. Neurosci 17, 962–970. [PubMed: 24908103]
29. Ribeiro IMA, Drews M, Bahl A, Machacek C, Borst A, and Dickson BJ (2018). Visual Projection Neurons Mediating Directed Courtship in Drosophila. Cell 174, 607–621.e18. [PubMed: 30033367]
30. Ache JM, Polsky J, Alghailani S, Parekh R, Breads P, Peek MY, Bock DD, von Reyn CR, and Card GM (2019). Neural Basis for Looming Size and Velocity Encoding in the Drosophila Giant Fiber Escape Pathway. Curr. Biol 29, 1073–1081.e4. [PubMed: 30827912]
31. Mongeau JM, Cheng KY, Aptekar J, and Frye MA (2019). Visuomotor strategies for object approach and aversion in Drosophila melanogaster. J. Exp. Biol 222.
32. Van Breugel F, and Dickinson MH (2012). The visual control of landing and obstacle avoidance in the fruit fly Drosophila melanogaster. J. Exp. Biol 215, 1783–1798. [PubMed: 22573757]
33. Maimon G, Straw AD, and Dickinson MH (2010). Active flight increases the gain of visual motion processing in Drosophila. Nat. Neurosci 13, 393–399. [PubMed: 20154683]
34. Cheng KY, Colbath RA, and Frye MA (2019). Olfactory and Neuromodulatory Signals Reverse Visual Object Avoidance to Approach in Drosophila. Curr. Biol 29, 2058–2065.e2. [PubMed: 31155354]
35. Mongeau JM, and Frye MA (2017). Drosophila Spatiotemporally Integrates Visual Signals to Control Saccades. Curr. Biol 27, 2901–2914.e2. [PubMed: 28943085]
36. Mronz M, and Lehmann FO (2008). The free-flight response of Drosophila to motion of the visual environment. J. Exp. Biol 211, 2026–2045. [PubMed: 18552291]
37. Strother JA, Wu ST, Rogers EM, Eliason JLM, Wong AM, Nern A, and Reiser MB (2018). Behavioral state modulates the on visual motion pathway of drosophila. Proc. Natl. Acad. Sci. U. S. A 115, E102–E111. [PubMed: 29255026]
38. Longden KD, and Krapp HG (2010). Octopaminergic Modulation of Temporal Frequency Coding in an Identified Optic Flow-Processing Interneuron. Front. Syst. Neurosci 4.
39. Suver MP, Mamiya A, and Dickinson MH (2012). Octopamine Neurons Mediate Flight-Induced Modulation of Visual Processing in Drosophila. Curr. Biol 22, 2294–2302. [PubMed: 23142045]
40. Jenett A, Rubin GM, Ngo TTB, Shepherd D, Murphy C, Dionne H, Pfeiffer BD, Cavallaro A, Hall D, Jeter J, et al. (2012). A GAL4-Driver Line Resource for Drosophila Neurobiology. Cell Rep 2, 991–1001. [PubMed: 23063364]
41. Keleş MF, Hardcastle BJ, Städele C, Qi X, and Frye MA (2020). Inhibitory interactions and columnar inputs to an object motion detector in Drosophila. Cell Rep in press.
42. Schnell B, Raghu SV, Nern A, and Borst A (2012). Columnar cells necessary for motion responses of wide-field visual interneurons in Drosophila. J. Comp. Physiol. A 198, 389–395.
43. Talay M, Richman EB, Snell NJ, Hartmann GG, Fisher JD, Sorkaç A, Santoyo JF, Chou-Freed C, Nair N, Johnson M, et al. (2017). Transsynaptic Mapping of Second-Order Taste Neurons in Flies by trans-Tango. Neuron 96, 783–795.e4. [PubMed: 29107518]
44. Enell L, Hamasaka Y, Kolodziejczyk A, and Nässel DR (2007). γ-Aminobutyric acid (GABA) signaling components in Drosophila : Immunocytochemical localization of GABA B receptors in relation to the GABA A receptor subunit RDL and a vesicular GABA transporter. J. Comp. Neurol 505, 18–31. [PubMed: 17729251]
45. Mauss AS, Meier M, Serbe E, and Borst A (2014). Optogenetic and pharmacologic dissection of feedforward inhibition in Drosophila motion vision. J. Neurosci 34, 2254–2263. [PubMed: 24501364]
46. Nicolai LJJ, Ramaekers A, Raemaekers T, Drozdzecki A, Mauss AS, Yan J, Landgraf M, Annaert W, Hassan BA, Nicolaï LJJ, et al. (2010). Genetically encoded dendritic marker sheds light on neuronal connectivity in Drosophila. Proc. Natl. Acad. Sci 107, 20553–20558. [PubMed: 21059961]
47. Nern A, Pfeiffer BD, and Rubin GM (2015). Optimized tools for multicolor stochastic labeling reveal diverse stereotyped cell arrangements in the fly visual system. Proc. Natl. Acad. Sci. U. S. A 112, E2967–76. [PubMed: 25964354]

48. Dhande OS, Stafford BK, Franke K, El-Danaf R, Percival KA, Phan AH, Li P, Hansen BJ, Nguyen PL, Berens P, et al. (2019). Molecular fingerprinting of on–off direction-selective retinal ganglion cells across species and relevance to primate visual circuits. J. Neurosci 39, 78–95. [PubMed: 30377226]
49. Kim T, Soto F, and Kerschensteiner D (2015). An excitatory amacrine cell detects object motion and provides feature-selective input to ganglion cells in the mouse retina. Elife 4, e08025.
50. Ölveczky BP, Baccus SA, and Meister M (2003). Segregation of object and background motion in the retina. Nature 423, 401–408. [PubMed: 12754524]
51. Ache JM, Namiki S, Lee A, Branson K, and Card GM (2019). State-dependent decoupling of sensory and motor circuits underlies behavioral flexibility in Drosophila. Nat. Neurosci 22, 1132–1139. [PubMed: 31182867]
52. Evans PD, and Gee JD (1980). Action of formamidine pesticides on octopamine receptors. Nature 287, 60–62. [PubMed: 6251379]
53. Behnia R, Clark DA, Carter AG, Clandinin TR, and Desplan C (2014). Processing properties of on and off pathways for Drosophila motion detection. Nature 512, 427–430. [PubMed: 25043016]
54. Strother JA, Nern A, and Reiser MB (2014). Direct observation of on and off pathways in the drosophila visual system. Curr. Biol 24, 976–983. [PubMed: 24704075]
55. Joesch M, Schnell B, Raghu SV, Reiff DF, and Borst A (2010). ON and off pathways in Drosophila motion vision. Nature 468, 300–304. [PubMed: 21068841]
56. Maisak MS, Haag J, Ammer G, Serbe E, Meier M, Leonhardt A, Schilling T, Bahl A, Rubin GM, Nern A, et al. (2013). A directional tuning map of Drosophila elementary motion detectors. Nature 500, 212–216. [PubMed: 23925246]
57. Wiederman SD, Shoemaker PA, and O'Carroll DC (2008). A Model for the Detection of Moving Targets in Visual Clutter Inspired by Insect Physiology. PLoS One 3, e2784. [PubMed: 18665213]
58. Wiederman SD, Fabian JM, Dunbier JR, and O'Carroll DC (2017). A predictive focus of gain modulation encodes target trajectories in insect vision. Elife 6, e26478. [PubMed: 28738970]
59. Fisher YE, Silies M, and Clandinin TR (2015). Orientation Selectivity Sharpens Motion Detection in Drosophila. Neuron 88, 390–402. [PubMed: 26456048]
60. Gruntman E, Romani S, and Reiser MB (2018). Simple integration of fast excitation and offset, delayed inhibition computes directional selectivity in Drosophila. Nat. Neurosci 21, 250–257. [PubMed: 29311742]
61. Nordström K, Barnett PD, and O'Carroll DC (2006). Insect Detection of Small Targets Moving in Visual Clutter. PLoS Biol 4, e54. [PubMed: 16448249]
62. Takemura S.ya, Nern A, Chklovskii DB, Scheffer LK, Rubin GM, and Meinertzhagen IA (2017). The comprehensive connectome of a neural substrate for 'ON' motion detection in Drosophila. Elife 6.
63. Haag J, Mishra A, and Borst A (2017). A common directional tuning mechanism of Drosophila motion-sensing neurons in the ON and in the OFF pathway. Elife 6, e29044. [PubMed: 28829040]
64. Candy DJ (1978). The regulation of locust flight muscle metabolism by octopamine and other compounds. Insect Biochem 8, 177–181.
65. Arenz A, Drews MS, Richter FG, Ammer G, and Borst A (2017). The Temporal Tuning of the Drosophila Motion Detectors Is Determined by the Dynamics of Their Input Elements. Curr. Biol 27, 929–944. [PubMed: 28343964]
66. Strother JA, Wu ST, Wong AM, Nern A, Rogers EM, Le JQ, Rubin GM, and Reiser MB (2017). The Emergence of Directional Selectivity in the Visual Motion Pathway of Drosophila. Neuron 94, 168–182.e10. [PubMed: 28384470]
67. Geurten BRH, Nordström K, Sprayberry JDH, Bolzon DM, and O'Carroll DC (2007). Neural mechanisms underlying target detection in a dragonfly centrifugal neuron. J. Exp. Biol 210, 3277–3284. [PubMed: 17766305]
68. Wiederman SD, and O'Carroll DC (2011). Discrimination of features in natural scenes by a dragonfly neuron. J. Neurosci 31, 7141–7144. [PubMed: 21562276]
69. Luan H, Peabody NC, Vinson CRR, and White BH (2006). Refined Spatial Manipulation of Neuronal Function by Combinatorial Restriction of Transgene Expression. Neuron 52, 425–436. [PubMed: 17088209]

70. Pfeiffer BD, Jenett A, Hammonds AS, Ngo TTB, Misra S, Murphy C, Scully A, Carlson JW, Wan KH, Laverty TR, et al. (2008). Tools for neuroanatomy and neurogenetics in Drosophila. Proc. Natl. Acad. Sci. U. S. A 105, 9715–9720. [PubMed: 18621688]

71. Weir PT, and Dickinson MH (2015). Functional divisions for visual processing in the central brain of flying Drosophila. Proc. Natl. Acad. Sci. U. S. A 112, E5523–E5532. [PubMed: 26324910]

72. Reiser MB, and Dickinson MH (2008). A modular display system for insect behavioral neuroscience. J. Neurosci. Methods 167, 127–139. [PubMed: 17854905]

73. Omoto JJ, Keleş MF, Nguyen B-CM, Bolanos C, Lovick JK, Frye MA, and Hartenstein V (2017). Visual Input to the Drosophila Central Complex by Developmentally and Functionally Distinct Neuronal Populations. Curr. Biol 27, 1098–1110. [PubMed: 28366740]

74. Akin O, and Zipursky SL (2016). Frazzled promotes growth cone attachment at the source of a Netrin gradient in the Drosophila visual system. Elife 5,; 5:e20762.

75. Helfrich-Förster C (2007). Immunohistochemistry in Drosophila In Circadian Rhythms. Methods in Molecular Biology, Rosato E, ed., pp. 533–547. [PubMed: 17417039]

Highlights

- LC12 and LC15 are ON-OFF visual feature detectors
- LC15 responds to moving bars, whereas LC12 responds to objects of any size
- Object responses from both LCs are suppressed when the background is moving
- Octopamine restores object responses in LC12 and LC15 against a moving background

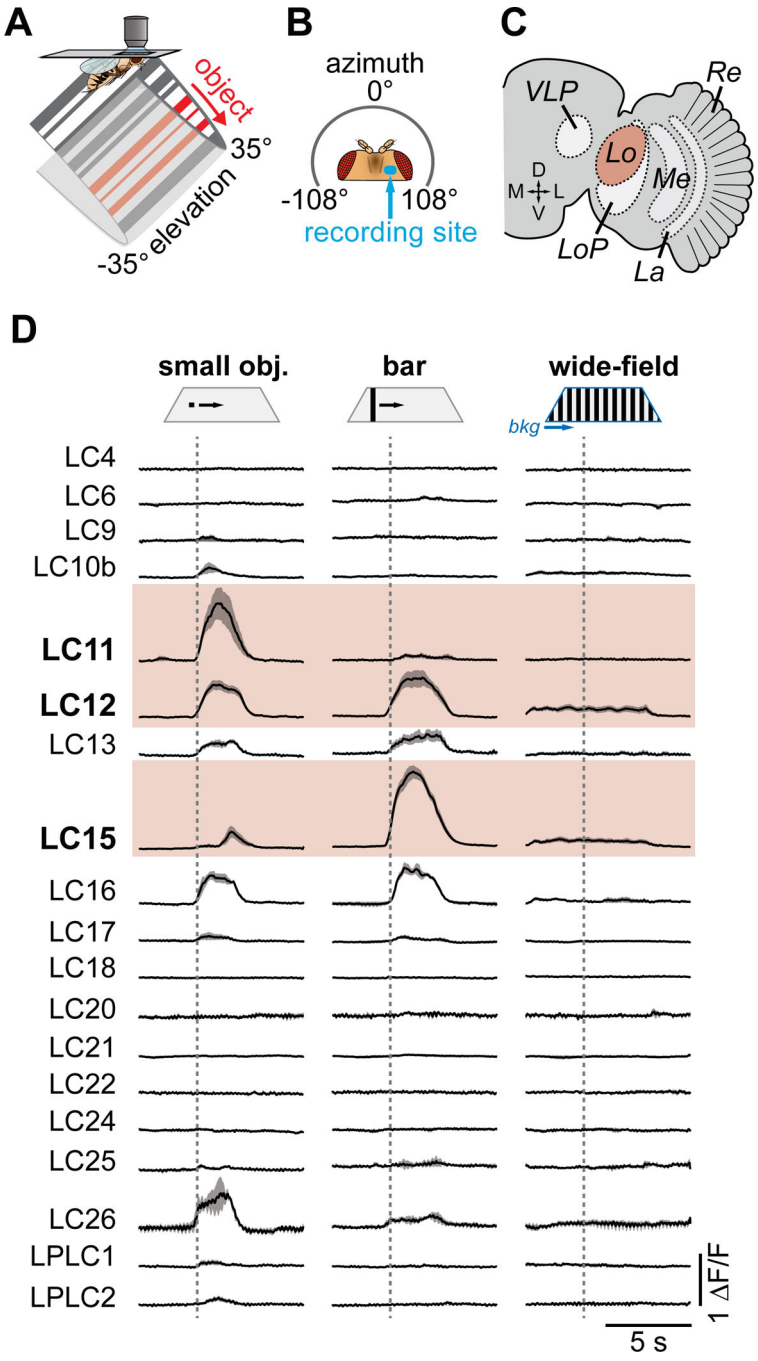

Figure 1. Few lobula columnar neurons respond to vertical bars or small objects.

(**A**) Two-photon calcium imaging. Head-fixed flies were presented with visual stimuli from a surrounding LED display. (**B**) Recordings were made from the right optic lobe. (**C**) Schematic of *Drosophila* optic lobe neuropils, with the lobula highlighted in red. (**D**) Mean (+/− SD shading) glomerular GCamp6f responses by LC neuron types to a moving solid 8.8×8.8° dark object, an 8.8×70° dark bar and wide-field grating (17.6° period). Visual stimuli are depicted at the top and moved from contra- to ipsilateral at 22°/s. Dashed lines indicate passing across the arena midline (0°). N = at least 5 flies for each LC type.

Re=retina, La=lamina, Me=medulla, LoP=lobula plate, Lo=lobula, VLP= ventrolateral protocerebrum. See also responses to motion defined stimuli in Figure S1.

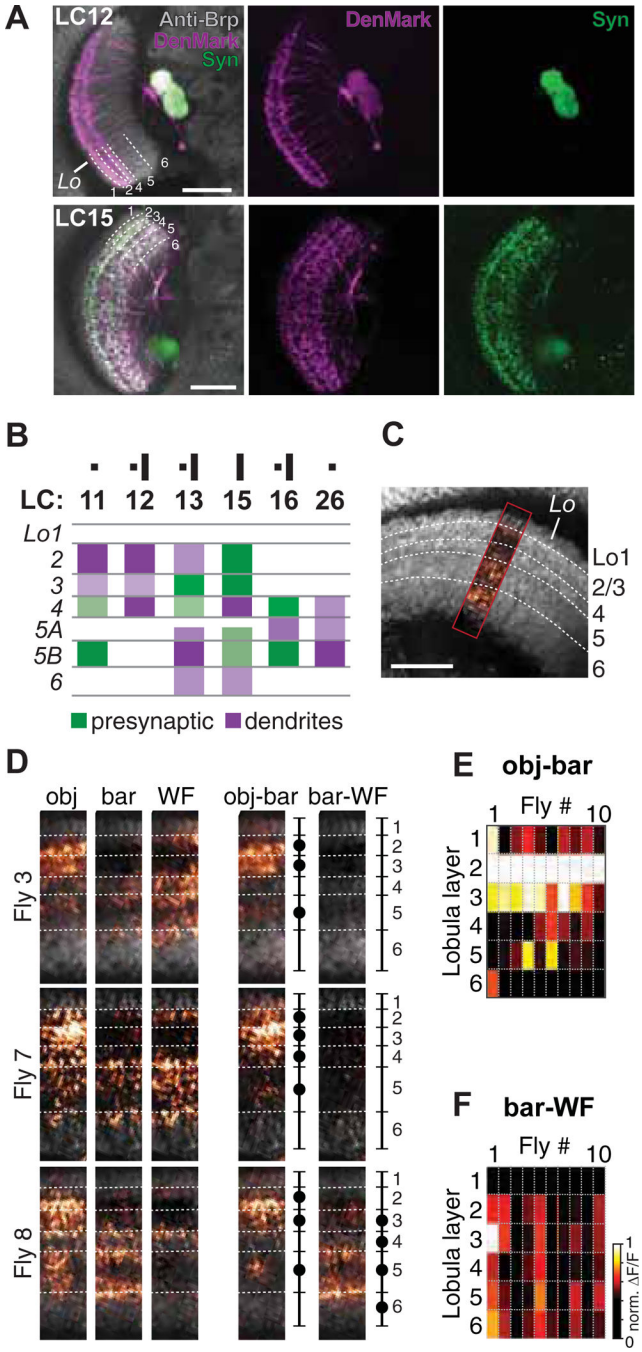

Figure 2. Presynaptic neuronal responses to small object motion is observed in lobula layer 2/3.

(**A**) Single plane confocal images of the anterior view of flies expressing DenMark and synaptically-tethered GFP (UAS-DenMark; UAS-syt.eGFP). Neuropil was labeled with anti-Bruchpilot antibody nc82 (gray). (**B**) Summary diagram of pre- and postsynaptic (dendritic) arbors of LC neuron types that showed responses to small objects and bars, reconstructed from DenMark and synaptotagmin staining. (**C-F**) Layer-specific small object input to the lobula. (**C**) Single plane confocal image illustrating the recording site (colored) used to determine layer specific lobula input. (**D**) Mean activity images of sytGCaMP6s expressed

in a pan neuronal driver (R57C10-GAL4) in response to a 8.8° object (obj.), a 8.8×70° bar, and 17.6° wide-field grating (WF) from three representative flies (see data from all flies in Figure S2). Approximate layer boundaries are indicated with dashed lines, constructed from high resolution images (gray). Schematics indicate innervated layers as filled circles. Obj-bar and bar-WF shows subtracted mean calcium response of the corresponding visual stimuli. (**E-F**) Layer specific input to the lobula for all tested flies (N=10), as maximum mean activity (norm ΔF/F) for each layer, normalized to the maximum response within a given fly.

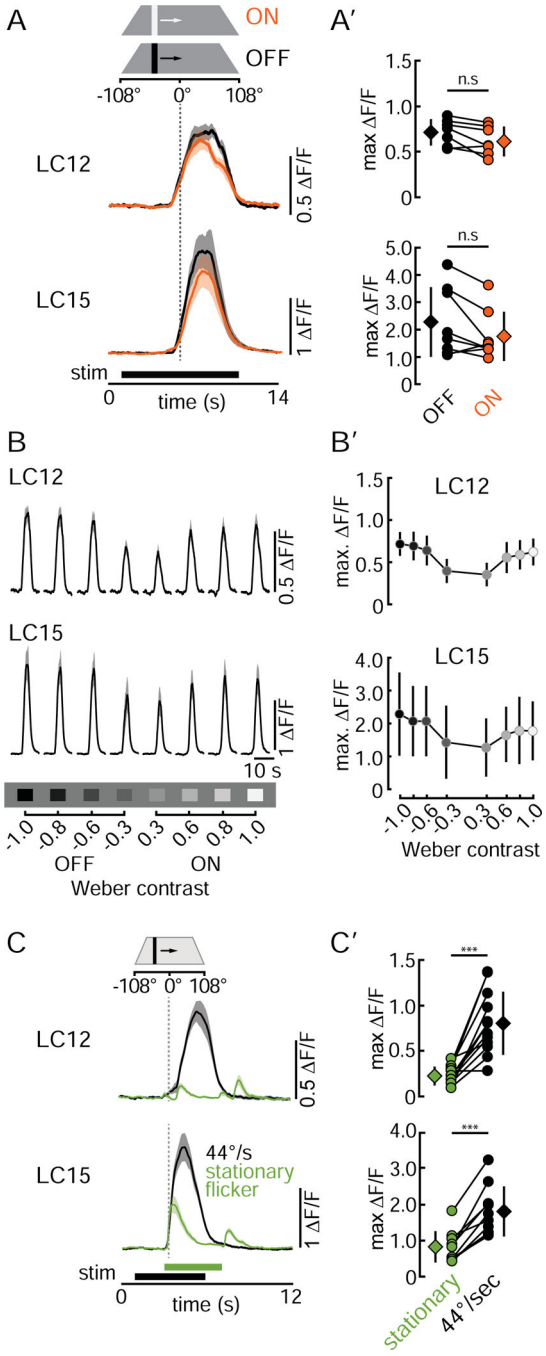

Figure 3. LC12 and LC15 are ON-OFF object motion detectors.

(**A**) Mean GCaMP6f signals (+/− SD shading) of LC12 and LC15 glomeruli in response to a bright (ON, orange) and dark (OFF, black) bar (8.8×70°, moved at 22°/s). (**A'**) Pairwise comparison of LC12 and LC15 OFF/ON maximum ΔF/F responses. Circles represent the mean of three repetitions of individual animals, diamonds present the mean across all animals tested +/−SD. n.s. = not significant. LC12: N=7 flies, LC15: N=8 flies. Statistics: paired t-test, LC12: t(6) = 2.74, p = 0.064, LC15: t(7)= 2.15, p = 0.069. (**B**) Mean GCaMP6f signal of LC12 and LC15 glomeruli in response to varying contrast bars (8.8×70°, 22°/s).

(**B'**) Comparison of LC12 and LC15 contrast selectivity. Fill color of circles represents the bar luminance. Circles represent the mean +/−SD across all animals. LC12: N=7 flies, LC15: N=8 flies. (**C**) Mean GCaMP6f glomeruli signals in response to an 8.8×70° stationary flickering bar (green) appearing and disappearing at +26° on the display, and the same bar moving with 44°/s (black). LC12: N=12 flies, LC15: N=10 flies. (**C'**) Pairwise comparison of maximum peak responses of the data shown in (C). Circles represent individual animals, diamonds depict the mean +/−SD. Statistics: paired t-test. LC12: t(11) = 5.97, p = 9.35e-05, LC15: t(9) = 7.47, p = 3.81e-05. See summary in Table S1.

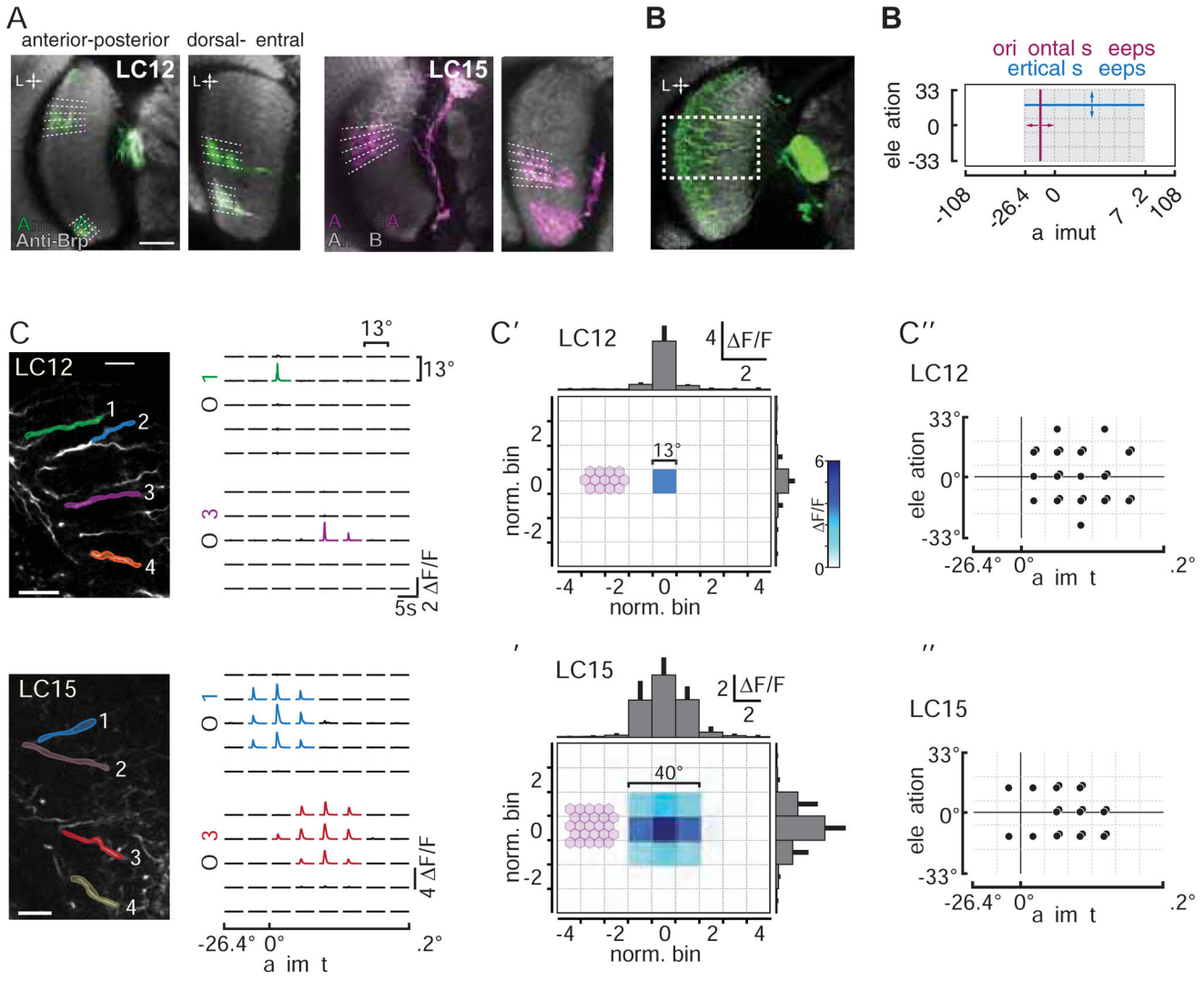

Figure 4. LC15 has a larger receptive field than LC12.

(**A**) Spatial distribution of LC12 and LC15 arbors in the lobula. Single layer confocal images of stochastically labeled LC12 and LC15 neurons (MCFO-1). Lobula columns indicated with dashed lines. D=dorsal, V=ventral, M=medial, L=lateral, A=anterior, P=posterior. Scale bars, 25 μm. (**B**) Single confocal plane image of LC12 in the anterior view illustrating the recording site (dashed rectangle). (**B'**) Representation of visual stimuli used to scan the RF. The gray highlighted region of the display was divided into 13.2° spaced bins within which a 2.2° dark bar stimulus was moved in all four cardinal directions (up, down, left, right, 22°/s). (**C, D**) Single cell RF mapping from representative flies. Left: Single neurite regions of interest overlaid on single plane two-photon images. Scale bars, 5 μm. Right: Multiplied calcium traces from representative LC12 and LC15 recordings arranged in a grid corresponding to (B'). (**C', D'**) Mean functional RF size of all tested flies, where bin # 0 represents the RF center. Histograms show the mean peak GCaMP6f responses +/−SD for each normalized bin. LC12: N=8 flies, n=26 neurites, LC15: N=5 flies, n=20 neurites. Purple sphere indicates the average anatomical RF depicted as retinal ommatidia corresponding to individual lobula columns. (**C", D"**) Spatial distribution of RF centers of

the cells included in C’ and D’ arranged in a grid corresponding to (B). Dots represent individual cells. See summary in Table S1.

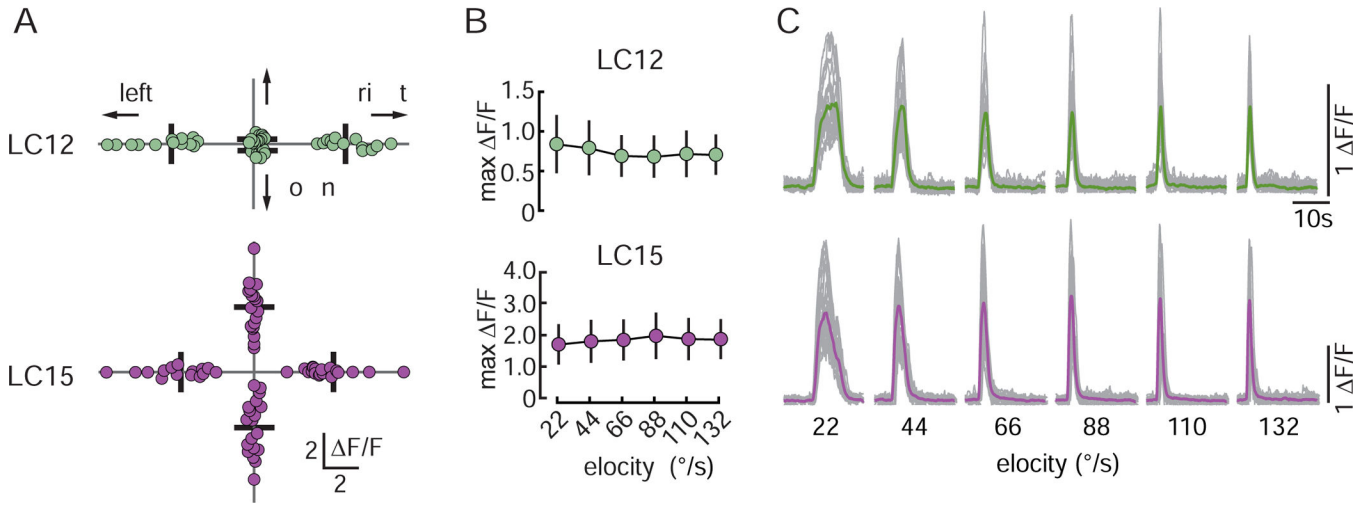

Figure 5. Neither LC12 nor LC15 are selective for stimulus direction or velocity.

(**A**) Directional tuning analysis of the data shown in Figure 4C'–D" Each dot represents the maximum ΔF/F response of individual cells to a 2.2° dark bar stimulus moving in the four cardinal directions (22°/s velocity). Bars indicate mean. LC12: N=8 flies, n=26 neurites, LC15: N=5 flies, n=20 neurites. (**B**) Responses of LC12 and LC15 to an 8.8×70° dark bar moving at 22–132°/s. Circles represent mean +/−SD. LC12: N=12 flies, LC15: N=10 flies. Responses were not statistical significant from each other (one way ANOVA, LC12: LC12: F(5,66)=0.561, p=0.729, LC15: F(5,54)=0.175, p=0.970). (**C**) Thin gray traces represent GCaMP6f responses of individual flies (three trials averaged), and thick colored traces show the mean across all animals tested to a 8.8×70° dark bar moving at 22–132°/s. LC12: N=12 flies, LC15: N=10 flies. See summary in Table S1.

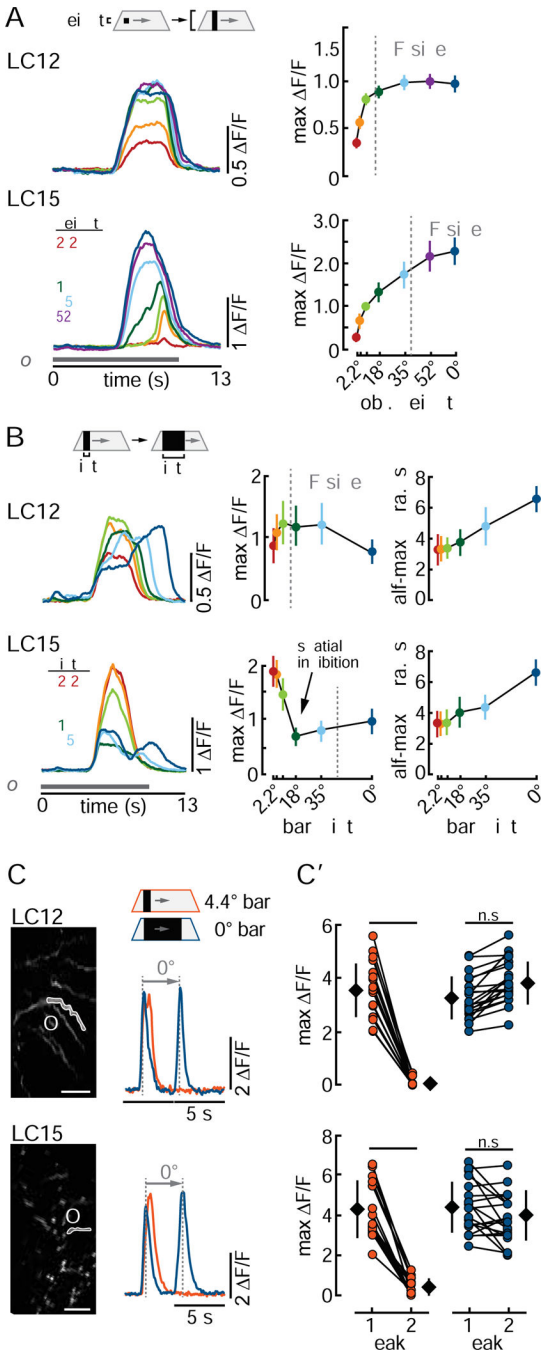

Figure 6. LC12 is an edge detector with spatial saturation and LC15 is a narrow-bar detector with spatial inhibition.

(**A-B**) Mean maximum glomerular calcium responses to (**A**) varying bar height (**B**) and varying bar width (velocity: 22°/s). Left: Mean responses +/−SD for LC12 (N=9 flies) and LC15 (N=10 flies). Vertical dashed lines indicate receptive field (RF) size. (**C**) Representative dendritic responses of individual neurites to a 4.4° (orange) and 70° (blue) wide bar. (**C'**) Pairwise comparison of maximum responses across animals. Circles represent single cells, diamonds depict mean responses +/−SD. n.s. = not significant. LC12: N=7 flies, n=20 dendrites, LC15: N=7 flies, n=19 dendrites. Statistics: paired t-test, LC12: 4.4°: t(19) =

16.39, p = 1.15e-12, 70°: t(19) = −2.98, p = 0.054; LC15: 4.4°: t(18) = 12.451, p = 2.78e-10, 70°: t(18) = 2.32, p= 0.062. Scale bars, 5 μm. See summary in Table S1.

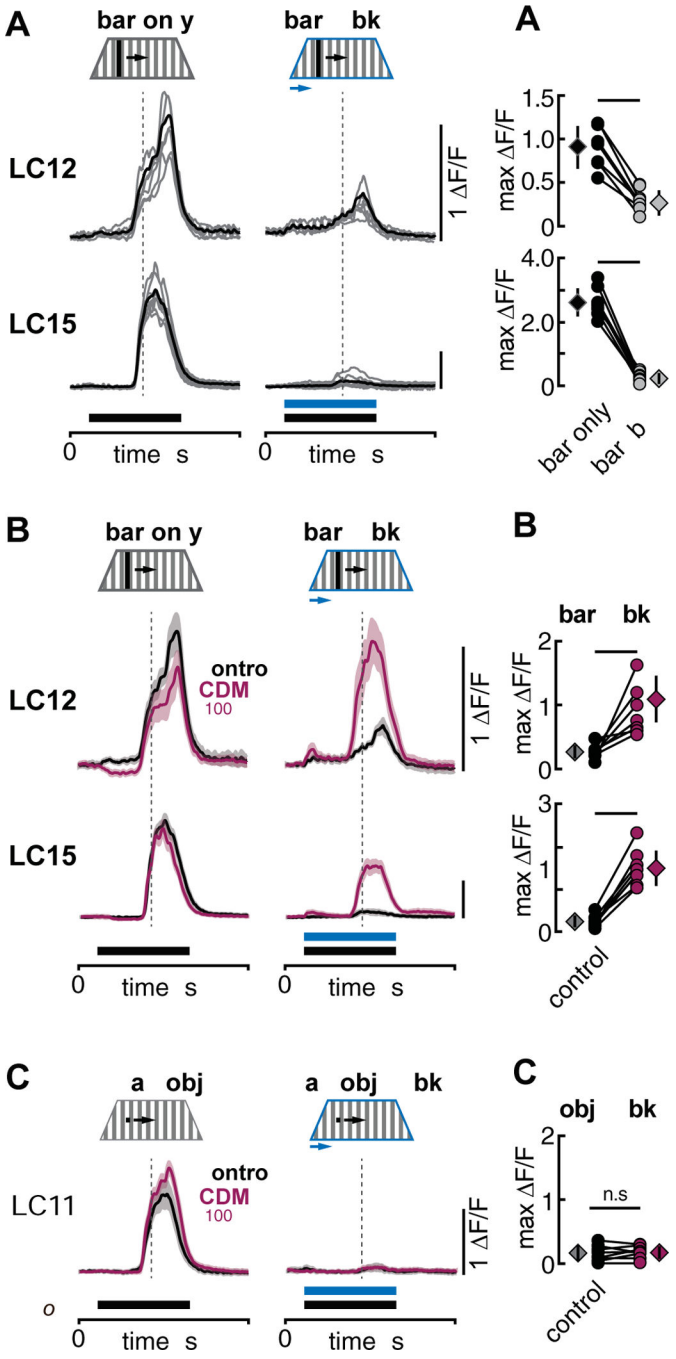

Figure 7. Octopaminergic modulation enables object detection against background motion in LC12 and LC15 but not in LC11.

(**A**) Glomerular GCaMP6f responses of LC12 and LC15 in response to an 8.8×70° dark bar moving contra- to ipsilateral with 44°/s over a stationary background (bar only) and both bar and wide-field background moving 44°/s from contra- to ipsilateral (bar + bkg). Gray traces represent individual flies while black traces show the mean across all animals tested. Time of bar and background movement is indicated with solid horizontal bars. Dashed vertical lines indicate the time when visual stimuli passed the arena midline. LC12: N=7 flies, LC15:

N=8 flies. (**A'**) Pairwise comparison of maximum 'F/F of traces shown in A. Circles represent individual flies while diamonds show mean +/− SD. Paired t-test, LC12: t(6) = 5.47, p = 0.0009, LC15: t(7) = 14.97, p = 1.42e-06. (**B, B'**) Same as A but mean GCaMP6f responses (+/− SD shaded) for LC12 and LC15 in control condition (saline, black) and in the presence of 100 μM CDM (magenta). LC12: N=7 flies, LC15: N=8 flies. Paired t-test, LC12: t(6) = −3.03, p = 0.019, LC15: t(7) = −10.47, p = 1.58e-05. (**C, C'**) Same as B but LC11 responses to an 8.8×8.8° dark small object. N=8 flies, paired t-test, LC11: t(7) = −0.61, p = 0.56. See data from both horizontal stimulus directions in Figure S3.

KEY RESOURCES TABLE

REAGENT or RESOURCE	SOURCE	IDENTIFIER
Antibodies		
anti-brp mouse monoclonal antibody	Developmental Studies Hybridoma Bank	Nc82 (supernatant) RRID:AB_2314866
anti-DsRed rabbit polyclonal antibody	Takara	632496, RRID:AB_10013483
anti-GFP chicken polyclonal antibody	abcam	ab13970, RRID:AB_300798
anti-HA rabbit monoclonal antibody	Cell Signaling Technologies	3724S, RRID:AB_1549585
anti-FLAG rat monoclonal antibody	Novus Biologicals	NBP1–06712 RRID: AB_1625981
Alexa Fluor 488, goat anti-chicken	abcam	ab150169, RRID:AB_2636803
Alexa Fluor 488, goat anti-rabbit	ThermoFisher Scientific	A-11008, RRID:AB_143165
Alexa Fluor 568, goat anti-rabbit	ThermoFisher Scientific	A-11036, RRID:AB_10563566
Alexa Fluor 594, goat anti-rat	Jackson Immuno Research Lab	112-585-167 RRID:AB_2338383
Alexa Fluor 647, goat anti-mouse	ThermoFisher Scientific	A-21236, RRID:AB_141725
Chemicals, Peptides, and Recombinant Proteins		
Chlordimeform	Sigma-Aldrich	31099; CAS: 6164-98-3
Deposited Data		
Deposited Data	Mendeley Data	doi: 10.17632/ssgpb4wmh9.1
Experimental Models: Organisms/Strains		
LC4: *R47H03-p65.AD(attP40); R72E01-GAL4.DBD(attP2), driver line*	Bloomington Drosophila Stock Center [12]	RRID:BDSC_68259 Janelia ID: SS00315
LC6: *R92B02-p65.AD(attP40); R41C07-GAL4.DBD(attP2),* driver line	Bloomington Drosophila Stock Center [12]	RRID:BDSC_68247 Janelia ID: OL0077B
LC9: *VT032961-p65.AD(attP40); VT040569-GAL4.DBD(attP2),* driver line	Bloomington Drosophila Stock Center [12]	RRID:BDSC_68342 Janelia ID: SS02651
LC10: *R35D04-p65.AD(attP40); R71E06.DBD(attP2),* driver line	Bloomington Drosophila Stock Center [12]	RRID:BDSC_68378 Janelia ID: SS00938
LC11: *R22H02-p65.AD(attP40); R20G06-Gal4.DBD(attP2),* driver line	Bloomington Drosophila Stock Center [12]	RRID:BDCS_68362 Janelia ID: OL0015B
LC12: *R35D04-p65.AD(attP40); R65B05-GAL4.DBD(attP2),* driver line	Bloomington Drosophila Stock Center [12]	RRID: BDSC_68352 Janelia ID: OL0007B
LC12: *R35D04-p65.AD(attP40); R55F01-GAL4.DBD(attP2),* driver line	Bloomington Drosophila Stock Center [12]	RRID:BDSC_68353 Janelia ID: OL0008B
LC13: *R14A11-p65.AD(attP40); R50C10-GAL4.DBD(attP2),* driver line	Bloomington Drosophila Stock Center [12]	RRID:BDSC_68257 Janelia ID: OL0027B
LC15: *R26A03-p65.AD(attP40); R24A02-GAL4.DBD(attP2),* driver line	Bloomington Drosophila Stock Center [12]	RRID:BDSC_68258 Janelia ID: OL0042B
LC16: *R26A03-p65.AD(attP40); R54A05-GAL4.DBD(attP2),* driver line	Bloomington Drosophila Stock Center [12]	RRID:BDSC_68331 Janelia ID: OL0046B
LC17: *R21D03-p65.AD(attP40); [R65C12-GAL4.DBD(attP2),* driver line	Bloomington Drosophila Stock Center [12]	RRID:BDSC_68356 Janelia ID: OL0005B
LC18: *R92B11-p65.AD(attP40); R82D11-GAL4.DBD(attP2),* driver line	Bloomington Drosophila Stock Center [12]	RRID:BDSC_68358 Janelia ID: OL0010B
LC20: *R35B06-GAL4.DBD(attP2); R17A04-p65.AD(VK00027),* driver line	Bloomington Drosophila Stock Center [12]	RRID:BDSC_68260 Janelia ID: SS00343

REAGENT or RESOURCE	SOURCE	IDENTIFIER
LC21: *R41C05-p65.AD(attP40); R55C04-GAL4.DBD(attP2)*, driver line	Bloomington Drosophila Stock Center [12]	RRID:BDSC_68330 Janelia ID: OL0045B
LC22: *R64G10-p65.AD(attP40); R35B06-GAL4.DBD(attP2)*, driver line	Bloomington Drosophila Stock Center [12]	RRID:BDSC_68357 Janelia ID: OL0001B
LC24: *VT038216-p65.AD(attP40); VT026477-GAL4.DBD(attP2)*, driver line	Bloomington Drosophila Stock Center [12]	RRID:BDSC_68340 Janelia ID: SS02638
LC25: *VT009792-p65.AD(attP40); VT002021-GAL4.DBD(attP2)*, driver line	Bloomington Drosophila Stock Center [12]	RRID:BDSC_68341 Janelia ID: SS02650
LC26: *VT007747-p65.AD(attP40); R85H06-GAL4.DBD(attP2)*, driver line	Bloomington Drosophila Stock Center [12]	RRID:BDSC_68333 Janelia ID: SS02445
LPLC1: *R64G09-p65.AD(attP40); R37H04-GAL4.DBD(attP2)*, driver line	Janelia Research Campus [12]	Janelia ID: OL0029B
LPLC2: *R19G02-p65.AD(attP40); R75G12-GAL4.DBD(attP2)*, driver line	Janelia Research Campus [12]	Janelia ID: OL0048B
Pan neuronal: *GMR57C10-GAL4(attP2)*, driver line	Bloomington Drosophila Stock Center	RRID:BDSC_39171
GFP: *10XUAS-IVS-mCD8::GFP(attP2)*, effector line	Bloomington Drosophila Stock Center	RRID:BDSC_32185
GCaMP: *20xUAS-IVS-GCaMP6f(attP40)*, effector line	Bloomington Drosophila Stock Center	RRID:BDSC_42747
sytGCaMP: *UAS-sytGCaMP6s(attP40)*, effector line	Bloomington Drosophila Stock Center	RRID:BDSC_64415
UAS-DenMark; UAS-syt.eGFP, effector line	Bloomington Drosophila Stock Center [46]	RRID:BDSC_33064
MCFO: *pBPhsFlp2::PEST (attP3); pJFRC201-10XUAS-FRT > STOP > FRT-myr::smGFP-HA (VK0005), pJFRC240–10XUAS-FRT > STOP > FRT-myr::smGFP-V5-THS-10XUAS-FRT > STOP > FRT-myr::smGFP-FLAG (su(Hw)attP1)*, effector line	Bloomington Drosophila Stock Center [47]	RRID:BDSC_64085
Software and Algorithms		
MATLAB R2019a	MathWorks	https://www.mathworks.com/
Adobe Illustrator CS6	Adobe Systems Inc.	RRID:SCR_010279 http://www.adobe.com/products/illustrator.html
MATLAB analysis code	B. Hardcastle	https://github.com/bjhardcastle/SlidebookObj
Fiji	Rasband, W.S, national Institutes of Health	RRID:SCR_002285 http://fiji.sc
SlideBook6	Intelligent Imaging Innovations Inc. (3i)	RRID:SCR_014300 https://www.intelligent-imaging.com/slidebook